Isoreticular Expansion in Porous Al(III) and Ga(III) Phosphonates: Synthesis, Structure, and Properties

Non Peer-reviewed author version

THEISSEN, Jennifer; Radke, Marvin; Mangelsen, Sebastian; DERVEAUX, Elien; Narváez Adams, Roberth Mateo; Lopau, Jasper; Näther, Christian; Nelle, Christian; Struve, Jörn; Steinke, Felix; Gys, Nick; Tielens, Frederik; ADRIAENSENS, Peter; Henke, Sebastian; MARCHAL, Wouter; Ameloot, Rob & Stock, Norbert (2025)
Isoreticular Expansion in Porous Al(III) and Ga(III) Phosphonates: Synthesis, Structure, and Properties.

DOI: 10.26434/chemrxiv-2025-jd1sk
Handle: http://hdl.handle.net/1942/48257

Isoreticular Expansion in Porous Al(III) and Ga(III) Phosphonates: Synthesis, Structure, and Properties

Jennifer Theissen[+[a,b]], Marvin Radke[+[c]], Sebastian Mangelsen[[c]], Elien Derveaux[[b]], Roberth Mateo Narváez Adams[[d]], Jasper Lopau[[c]], Christian Näther[[c]], Christian Nelle[[e]], Jörn Struve[[c]], Felix Steinke[[c]], Nick Gys[[a]], Frederik Tielens[[d]], Peter Adriaensens[[b]], Sebastian Henke[[e]], Wouter Marchal*[[b]], Rob Ameloot*[[a]] and Norbert Stock*[[c]]

Affiliations

[a] Centre for Membrane Separations, Adsorption, Catalysis, and Spectroscopy (cMACS)
KU Leuven (Arenberg)
Celestijnenlaan 200F
3001 Leuven
Belgium

[b] Institute for Materials Research (IMO-IMOMEC), Analytical and Circular Chemistry (ACC)
NMR group
Hasselt University
Agoralaan Building D
3590 Diepenbeek
Belgium

[c] Institut für Anorganische Chemie
Christian-Albrechts-Universität zu Kiel
24118 Kiel
Germany

[d] Department of General Chemistry (ALGC) – Materials Modelling Group
Vrije Universiteit Brussels
Pleinlaan 2
1050 Brussels, Belgium

[e] Department of Chemistry and Chemical Biology
TU Dortmund
Otto-Hahn-Str. 6
44227 Dortmund, Germany

+ Co-first authors, contributed equally

* Corresponding Author, E-mail: stock@ac.uni-kiel.de, rob.ameloot@kuleuven.be, wouter.marchal@uhasselt.be

Supporting information for this article are given via a link at the end of the document.

Keywords: Metal-Organic Framework • Metal Phosphonate • Porosity • Isoreticular Chemistry

SYNOPSIS

Two phosphonate-based metal-organic frameworks, with framework composition [M(OH)(H_2BPD)] xH_2O (M = Al^{3+}, Ga^{3+}, H_4BPD = *N, N'*-4,4'-bipiperidine-bis(methylenephosphonic acid), denoted as M-CAU-67, adopt an expanded MIL-91 structure. Structural and sorption data revealed framework flexibility and permanent porosity, illustrating a rare example of successful isoreticular expansion in metal phosphonates.

ABSTRACT

We report the synthesis and structural elucidation of two metal-organic frameworks (MOFs), [M(OH)(H_2BPD)]·xH_2O (M = Al^{3+}, Ga^{3+}), denoted as M-CAU-67, synthesized using the ditopic linker molecule *N, N'*-4,4'-bipiperidine-bis(methylenephosphonic acid) (H_4BPD). The compounds were synthesized via hydrothermal synthesis and upscaling to the gram scale was achieved under reflux conditions, demonstrating the versatility in preparation. Single-crystal X-ray diffraction (SCXRD) revealed an isoreticular, expanded MIL-91 structure, representing a rare case of successful isoreticular expansion in porous metal phosphonates. The framework structure was confirmed by Rietveld refinement against powder X-ray diffraction (PXRD) data. Comprehensive characterization, including solid-state NMR spectroscopy (^{31}P, ^{27}Al MQMAS) supports the structure model. Solvent exchange experiments, as well as variable-humidity/temperature PXRD data, revealed high flexibility with ΔV/V = 32 % between hydrated and activated states. The compounds are permanently microporous and show a complex, polarity- and size-dependent sorption behavior toward gases and vapors.

INTRODUCTION

Metal-organic frameworks (MOFs) have emerged as a versatile class of materials, due to their modular construction from inorganic building units (IBUs), such as metal ions or metal-oxo clusters, and organic linker molecules, commonly carboxylates or imidazolates.[1,2] Their remarkable structural diversity and functional versatility have led to a wide range of applications, including proton conductivity[3,4], ion exchange[5], catalysis[6,7], water harvesting[8], gas storage and separation[9]. In contrast to the vast number of carboxylate- and imidazolate-based MOFs, phosphonate-based frameworks remain underexplored: only 2.3 % of the structures in the MOF subset of the Cambridge Structural Database[10] (CSD; July 2025) are derived from phosphonic acids.

These porous metal phosphonates (PMPs) offer distinct advantages, including exceptional thermal[11,12] and chemical[4,7] stability, attributed to strong metal-phosphonate (P-O-M) bonds and the high coordination flexibility of phosphonate ligands, rendering PMPs suitable for a wider array of applications.[13,14] However, the synthesis of crystalline, porous PMPs remained challenging due to various reasons further limiting the discovery efforts:[15] (1) Uncontrolled nucleation; compared to C-O-

M interactions, the stronger P-O-M interactions impede a controlled self-assembly process during nucleation and crystallization, often resulting in fast precipitation and therefore the formation of non-crystalline materials or the absence of single crystals suitable for X-ray diffraction (SCXRD) analysis[16]; (2) hard to predict coordination behavior linked to variable deprotonation states and multiple coordination modes;[13,17] (3) general tendency toward dense, non-porous layer formation, due to the multiple coordination modes;[13,17] (4) limited commercial availability of the phosphonate linker molecules compared to carboxylate and imidazolate linkers and (5) often required multi-step synthesis of linkers. These challenges are reflected in the small number of reported crystalline and porous phosphonate MOFs. Despite aluminum's properties, including high charge density ($r(Al^{3+})$=53.5 pm)[18], abundance[19,20], low toxicity[21], and strong affinity for oxygen donors[22] only eight examples (SI, Tab. S1) of crystalline and porous phosphonate MOFs have been reported over the past three decades.

Until the early 2000s, reports of PMPs remained relatively scarce.[14] Among the most prominent early examples employing monophosphonic acids were the Zr(O_3P-Ph)[23,24], β-Cu(O_3P-CH_3)[25], AlMepO-α[26] and -β[26] ($Al_2(O_3PCH_3)_3$). The use of ditopic phosphonic acids to link adjacent layers frequently led to the formation of dense, non-porous structures. Strategies involving mixed linker systems, including monophosphonates or phosphates, introduced some porosity but often at the expense of crystallinity and broad pore size distributions due to the stochastic nature of defect formation.[27,28] More refined approaches, such as the "column-with-base" strategy developed by Alberti et al.[27], leveraged aromatic diphosphonates bearing sterically demanding substituents (-CH_3, -OH, -COOH) close to the phosphonate moieties to achieve well-defined porous structures with improved crystallinity and narrower pore size distributions.[27,29] The incorporation of additional functional groups – such as tertiary amines in piperazine- and bipiperidine-derived linkers – further expanded the PMP landscape, resulting in a series of frameworks reported throughout the early 2000s and 2010s. A milestone was reached in 2006 when Serre *et al.*[30] reported MIL-91, the first porous metal phosphonate constructed from *N,N*'-piperazine-bis(methylene phosphonic acid) (H_4PMP), incorporating tri- and tetravalent metal cations (Al^{3+} and Ti^{4+}).[30] MIL-91 exhibits well-defined, narrow pores and notable CO_2 adsorption capacities, thereby highlighting the potential of PMPs in gas storage and separation technologies.[30,31] Isostructurality in phosphonate-based frameworks has been demonstrated when metals of identical or different valencies are exchanged. Examples include the previously mentioned MIL-91[30], but also STA-12[32], STA-16[32], CAU-53[33] CAU-60[34] and CALF-41[35] among others. When metals of different oxidation states are involved, charge compensation is usually achieved by varying degrees of framework protonation. Isostructural phases can also be obtained by employing either the free phosphonic acid or its monoester derivative, as observed for CALF-33.[36]

To address the limitations of narrow pore structures, researchers have turned to isoreticular chemistry – systematic linker extension while retaining topology – as a promising approach for the rational design of large-pore MOFs.[37,38] While isoreticular design has driven significant advances in carboxylate MOFs, its application to PMPs has been hindered by the intrinsic coordination unpredictability of phosphonates.[39] Reports of isoreticular expansion through an increase in linker size in PMPs are extremely rare, especially in permanently porous compounds with substantial enlargement of the linker molecules, with STA-12[32] and STA-16[32] being the only examples in this field. Replacing H_4PMP (STA-12) with the elongated *N, N*'-4,4'-bipiperidine-bis(methylene phosphonic acid) (H_4BPD) yielded STA-16, which notably exhibited a significant increase in pore size and internal surface.[32] Nevertheless, it should be pointed out that alkyl bisphosphonates of divalent metal ions can vary greatly in structure, and sometimes porous or even isoreticular compounds are reported, *i.e.,* the Zink alkyl bisphosphonates, reported by the Clearfield group among others.[13,40] While the use of trivalent metal Ions often leads to nonporous or poorly crystalline compounds.[13,41,42] Recently, a minireview emphasized the structural similarities of IBUs in PMPs and stressed the difficulties of identifying appropriate synthesis conditions that produce the same IBU when the phosphonic acid is changed.[43] The limited number of isostructural expanded PMPs represents a significant limitation in the field. As a result, progress in expanding the structural and functional diversity of PMPs remains constrained, highlighting the need for comprehensive studies.

In this work, we extend the concept of isoreticular expansion, reporting M-CAU-67 (M = Al^{3+}, Ga^{3+}), based on the extended H_4BPD linker. The frameworks adopt a MIL-91-type structure with expanded pore size. Their synthesis was achieved via a high-throughput approach, and phase-pure compounds were synthesized under different synthetic conditions. The frameworks display significant structural flexibility in response to hydration and dehydration, as revealed by variable-temperature (VT-) and humidity-controlled PXRD (RH-PXRD) measurements.

RESULTS AND DISCUSSION

SYNTHESIS AND SAMPLE TREATMENT

The aluminum-based framework Al-CAU-67, $[(Al(OH)(H_2BPD)] \cdot 11\ H_2O$, was discovered through a systematic high-throughput investigation, involving $AlCl_3$, the linker H_4BPD, additives, and multiple temperature–time protocols (Figure 1 and SI section 3.2). The linker molecule was synthesized using a modified literature procedure; details are given in the supporting information (SI section 3.1). Phase-pure formation of highly crystalline Al-CAU-67 was achieved by combining solid H_4BPD, water, aqueous solutions of NaOH and $AlCl_3$ in a molar ratio of Al^{3+} : H_4BPD : NaOH = 1.2 : 1 : 3. Hydrothermal synthesis at 135 °C yielded the compound after reaction times ranging from 10 minutes under continuous stirring in glass vessels to 36 h in PTFE-lined steel autoclaves. Microwave-assisted synthesis under

continuous stirring in glass vessels at the same temperature yielded a highly crystalline product within 6 h. Notably, scale-up was readily achieved under reflux conditions in a round-bottom flask (250 mL), yielding up to 2 g of product per batch. In all cases, Al-CAU-67 was obtained as a colorless, microcrystalline powder with various morphologies and particle sizes (up to 80 µm along the largest dimension), depending on the synthesis method. The largest crystals were obtained under static conditions in PTFE-lined autoclaves, while reactions under reflux and stirring resulted in the smallest crystals (up to 5 µm, Figure 1). Details are given in SI sections 3.3 and 4.6. The purity of Al-CAU-67 was confirmed by PXRD, infrared (IR) and NMR spectroscopy as well as elemental analysis. Analogous synthesis optimization procedures yielded the gallium analogue Ga-CAU-67; detailed data for this compound, which exhibits similar properties, are provided in the SI section 4.

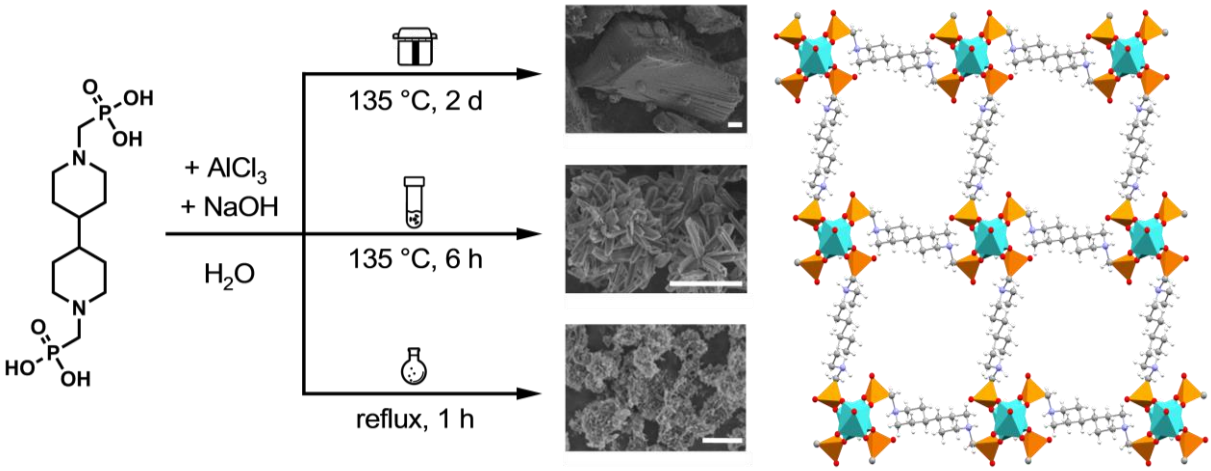

Figure 1: Summary of the synthesis conditions resulting in the formation of Al-CAU-67 - [(Al(OH)(H_2BPD)]. Different synthesis conditions under the same stoichiometric molar ratio of Al^{3+} : H_4BPD : NaOH = 1.2 : 1 : 3 led to different particle morphologies. Solvothermal synthesis at 135 °C for 2 d led to irregularly shaped block-like crystallites; microwave-assisted synthesis at 135 °C with constant stirring for 6 h led to homogeneous block-shaped crystallites; and reflux-based synthesis with constant stirring for 1 h led to very small, regularly shaped needles. The white scale in the SEM pictures is equal to 5 µm. Detailed conditions are given in the SI sections 3.3 and 4.6.

Samples collected immediately after the synthesis are referred to as **AS** (after synthesis). To render the pores accessible and prevent pore collapse upon removal of the water molecules due to capillary forces, solvent exchange was conducted using methanol (MeOH), ethanol (EtOH), and dichloromethane (DCM); samples subjected to this treatment are denoted as **SE** (solvent exchange). Recovery of the crystalline CAU-67 phase after thermal and mechanical treatment was achieved by refluxing the material in water for one hour. These samples are denoted as **Recycle**. Samples treated to improve crystallinity by reflux treatment are referred to as **Reflux**. Unless otherwise specified, all characterizations were performed on samples obtained from the microwave-assisted synthesis and were subjected to a reflux treatment.

STRUCTURE DETERMINATION AND DESCRIPTION

Although Al-CAU-67 was obtained as single crystals suitable for SCXRD, disordered water molecules in the pores prevented their localization in the electron density map, and their contribution was removed during the refinement of the SC data (Table 1). This omission resulted in a noticeable discrepancy between the observed and calculated intensities in the PXRD patterns (SI section 4.1). To model the arrangement of the water molecules in the pores, the crystal structure was refined against PXRD data. Based on the results of elemental and TG analyses of the same sample (SI section 4.3), eleven additional oxygen atoms corresponding to non-coordinated water molecules were introduced and subjected to global optimization using simulated annealing,[44] as implemented in TOPAS Academic V 6.0.[45] Repeated minima were found in which all solvent molecules take positions in the pore volume, not colliding with any of the framework atoms. No constraints had to be applied. Further, refinement of the linker molecules, which were modelled as rigid bodies with degrees of freedom for the torsion angles of the phosphonate group towards the aliphatic backbone, was performed. Only minor positional changes compared to the results of single-crystal structure determination were observed. The Rietveld refinement is in good agreement with measured PXRD data (Table 1, Figure 2). Refinement against pair distribution function (PDF) data revealed the overall same framework structure with differences due to the disordered solvent molecules (SI section 4.1.3).

Table 1: Summary of crystallographic data of Al-CAU-67 obtained by SCXRD analysis and Rietveld refinement against PXRD data.

SCXRD data		**PXRD data (Refined SCXRD data)**	
Parameter	**Value**	**Parameter**	**Value**
Empirical formula	$Al(OH)(C_{12}H_{24}N_2O_7P_2)$	**Empirical formula**	$Al(OH)(C_{12}H_{24}N_2O_7P_2)\cdot 11H_2O$
Formula weight	398.26	**Formula weight**	612.44
Temperature / K	100.00(11)	**Temperature / K**	293
Refinement	Least Squares	**Refinement**	Rietveld
Crystal system	triclinic	**Crystal system**	triclinic
Space group	*P-1*	**Space group**	*P-1*
***a* / Å**	6.85827(17)	***a* / Å**	6.83391(12)
***b* / Å**	14.5159(8)	***b* / Å**	14.6963(4)
***c* / Å**	14.9646(5)	***c* / Å**	14.9849(4)
***α* / °**	77.961(4)	***α* / °**	82.521(3)
***β* / °**	83.656(2)	***β* / °**	85.9141(18)
***γ* / °**	80.252(3)	***γ* / °**	79.119(3)
V / Å³	1431.60(10)	**V / Å³**	1463.67(6)
R_1 [I ≥ 2σ (I)]	0.0767	**R_{Bragg} / %**	0.641
wR_2	0.2284	***R_p* / %**	1.56
R_1 [all data]	0.0794	***R_{exp}* / %**	4.86
wR_2 [all data]	0.2320	***R_{wp}* / %**	2.03
GoF / %	1.058	**GoF / %**	0.41885

Al-CAU-67, [(Al(OH)(H_2BPD)]·11H_2O, crystallizes in a structure isoreticular to MIL-91(Al).[46] Structural details are shown in Figure 2. The asymmetric unit contains two Al^{3+} cations: one situated at the center of the unit cell and the other at the center of the *bc*-face, and one bridging OH group. Two symmetry-independent fragments of the linker molecule are oriented parallel to the *b*- and *c*-axes. Each Al^{3+} cation is sixfold coordinated, being surrounded by four oxygen atoms from four distinct phosphonate groups and two hydroxide ions, forming the IBU. The hydroxide ions (μ-OH) connect adjacent Al^{3+} ions, forming an infinite chain of *trans*-corner-sharing AlO_6-polyhedra extending along the *a*-axis (Figure 2 C). Each H_2BPD^{2-} linker bridges four Al^{3+} ions via its phosphonate groups, each coordinating two Al^{3+} ions within the same chain in a coordination mode described as [2.110] in Harris notation (Figure 2 B).[47] These two independent linker molecules expand the infinite chains into a three-dimensional coordination network along the *b*- and *c*-axes. The unidirectional rhombic channels show a limiting diameter of 8.74 Å and a maximum pore diameter of 9.26 Å (Figure 2 E). The topology of MIL-91 and CAU-67 is well known and is also observed in the metal carboxylates with MIL-53 structure. Depending on the representation of the vertices, the framework can be described either by an *sra* (4,4-net), *rna* (3,6-net) or *bqp* (4,6-net) topology.[48,49] In the *Cheetham*[50] notation for hybrid solids, the structure of all three MOFs can be described as a one-dimensional connected IBU, which is connected to two other dimensions via the organic linker, forming a three-dimensional framework, which is denoted I^1O^2.

According to the chemical formula [(Al(OH)(H_2BPD)]·11H_2O, two protons are present. As observed in MIL-91, these are located at the N atoms of the ring. This protonation is supported by SCXRD, FTIR, DRIFT and XPS spectroscopy (SI sections 4.1, 4.5 and 4.11). The ammonium groups form hydrogen bonds with the phosphonate oxygen atoms of neighboring linker molecules, which contributes additional stabilization to the structure. Two distinct donor-acceptor distances are observed: (1) N1-H···O12=P11 with an N1···O12 separation of 2.788(14) Å, and (2) N11-H···O2–P1 with a separation of 2.844(10) Å. Similar motifs are found in Al-MIL-91, where slightly shorter hydrogen bonds (2.564(9) Å, 2.597(7) Å) have been proposed to account for framework rigidity.[30,46] The longer hydrogen bond distances in Al-CAU-67 may contribute to its observed flexibility. Similar hydrogen bond interactions have also been reported in [ZrF_2(H_2PMP)] (d(O···N) = 2.61(12) Å)[51] and α-PCMOF21-Cl framework (d(O···N) = 2.733 Å).[52]

The structural data for CAU-67 obtained from Rietveld refinement against PXRD data and from SCXRD data have been deposited with the Cambridge Crystallographic Data Center (CCDC numbers 2452205, 2487365, 2487454).

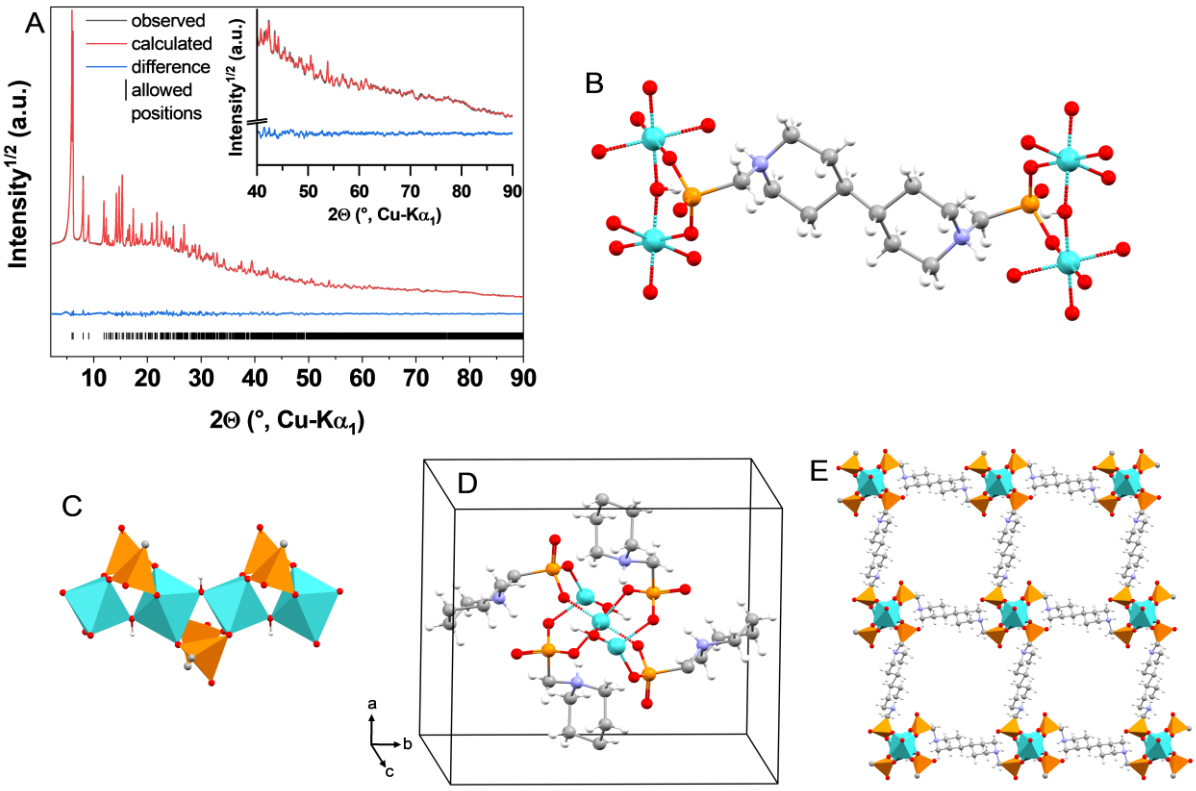

Figure 2: (A) Result of the Rietveld refinement against the XRPD data of Al-CAU-67. The measured PXRD pattern is shown in black, and the calculated one in red. The difference between the calculated and measured PXRD is shown in blue. Permitted reflection positions are shown as black vertical lines. The y-axis is scaled in root representation to make differences more visible. No additional reflections were observed. (B) Connectivity of a linker molecule to the aluminum ions. (C) Inorganic building unit (IBU) formed by the trans-corner-sharing AlO_6- and CPO_3-polyhedra along the *a*-axis with phosphonate-groups originating from different linker molecules. (D) unit cell and (E) pores of CAU-67 seen along the a-axis, oxygen molecules omitted for clarity. General color scheme: Al = turquoise, P = orange, O = red, N = purple, C = grey, H = white.

In order to understand the structural transformations of Al-CAU-67, it is crucial to clarify the role of water molecules within the framework and investigate how structural transformations upon activation are influenced. Accordingly, the thermal behavior of the material was examined using variable temperature powder X-ray diffraction (VT-PXRD), thermogravimetric and differential thermal analysis (TGA-DTA), differential scanning calorimetry (DSC) and temperature-dependent diffuse reflectance infrared Fourier transform spectroscopy (TD-DRIFTS). The behavior upon rehydration of the guest-free framework was investigated with water vapor sorption measurements and humidity-dependent PXRD experiments. Validation of the framework's structure was further achieved through solid-state nuclear magnetic resonance (ssNMR). This data will be presented in the following paragraphs.

THERMAL PROPERTIES

Mass losses associated with the desorption of guest molecules and the decomposition of the framework were monitored by DTA-TG. The **TG** data of Al-CAU-67 (Figure 3 (left, black line) and SI section 4.3) exhibited a small weight loss during equilibration at 30 °C under N_2 flow, followed by a two-step endothermic mass loss indicating the presence of two types of physisorbed water molecules residing in the one-dimensional channels with T_{end} = 90 °C and T_{end} = 150 °C, respectively. The combined mass loss (Δm_{sum} = 36 %) corresponds to the release of ≈13 H_2O molecules per formula unit ($\Delta m_{calc.}$ = 37 %). Starting at 150 °C, the TG curve exhibits a plateau, indicating the formation of an anhydrous framework that is thermally stable in this temperature range. Above 361 °C, the sample appears to thermally decompose (SI, section 4.3.3). The **DSC**-measurement (Figure 3 (left, white line) and SI section 4.4) shows two endothermic peaks associated with the stepwise evaporation of water guest molecules from the framework (ΔH ≈ 172 kJ mol^{-1} at T_{peak} ≈ 90 °C, and ΔH ≈ 38.4 kJ mol^{-1} at T_{peak} ≈ 149 °C). Both signals are confined to the initial up-scan; down-scans show no reversibility, and subsequent up-scans are featureless, consistent with formation of a stable anhydrous phase after the first heating cycle. **VT-PXRD** (Figure 3, left contour plot) revealed a series of structural transformations of Al-CAU-67 at approximately 40, 60, 95, 120, and 150 °C, which correlate with the dehydration events evidenced in the TG and DCS curves (Figure 3). We attribute the transformations to (1) reorganization of the hydrogen-bonding network of pore water during the initial heating stages, followed by (2) framework contraction upon guest removal to minimize empty pore volume. Upon dehydration, most reflections shift to higher 2θ values, consistent with contraction of the unit cell and the formation of a narrow-pore phase persisting up to 150 °C. Above that temperature, only a few reflections at low angles and otherwise diffuse scattering can be observed (Figure 3), pointing to a loss in long-range order. In contrast, some short-range order persists in the sample. **Temperature-dependent DRIFTS** provides additional support for the proposed steps (Figure 3, right). The bridging μ-OH stretching vibration at 3665 cm^{-1} remained observable up to 250 °C, confirming the integrity of the inorganic building units despite loss of crystallinity above 150 °C. The N-H stretching vibration at 2740 cm^{-1}, assigned to the tertiary ammonium cation of the linker molecule, is visible over the entire temperature range, indicating that the phosphonate remained coordinated to aluminum and is not protonated. With progressive dehydration, the water-related bands at 3350 cm^{-1} (O-H stretching) and 1655 cm^{-1} (H-O-H bending) diminish and disappear above 150 °C, consistent with the observation of a dehydrated form. Merging and broadening of vibrational modes in the fingerprint region above 150 °C further reflect the loss of long-range order and are attributed to vibrational broadening.

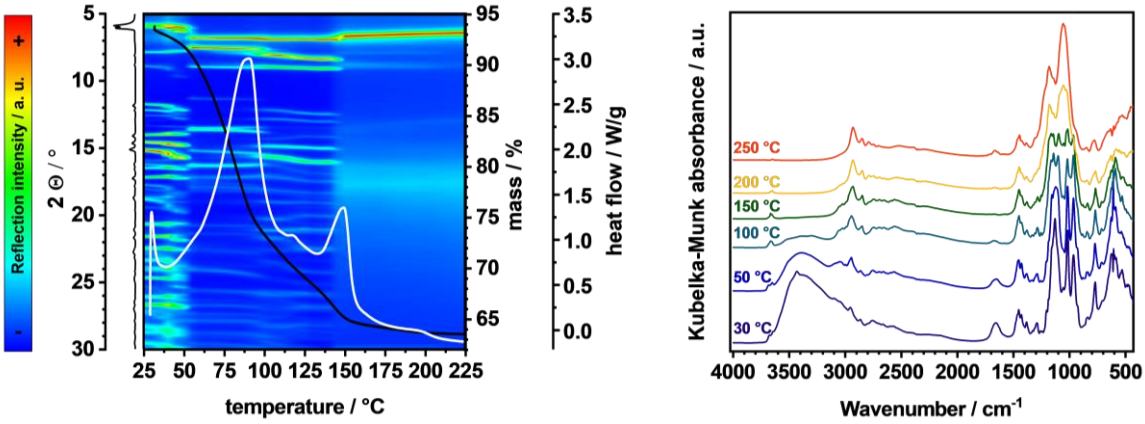

Figure 3: **Left**: Combination of the results of the VT-PXRD, TGA and DSC measurements. Contour plot of reflection intensity of VT-PXRD (color scale) as a function of 2Θ and temperature (y-axis, left). The black line represents the TGA mass-loss curve (first right y-axis), showing the removal of water molecules from the pores. The white curve (DSC signal, second right y-axis) shows the heat flow, exo down, highlighting the endothermic process of the release of the guest molecules. Multiple structural transformations into unknown crystalline phases are visible at 40, 60, 95, 116, and 150 °C, accompanied by systematic shifts of reflections and endothermic heat flow events. Above 150 °C, the long-range order is largely lost. **Right:** DRIFT spectra recorded at selected temperatures (offset for clarity). The μ-ν(O-H) at 3665 cm^{-1} remains visible up to 250 °C, indicating preservation of the inorganic building unit despite the decrease in long-range order. The loss of water molecules can be observed by the disappearance of the ν(O-H) (3350 cm^{-1}) and the δ(O-H) band (1655 cm^{-1}) between room temperature and 200 °C. The merging of bands in the fingerprint region is attributed to vibrational broadening.

In contrast, Al-MIL-91 undergoes only minor unit-cell changes upon heating.[30] This pronounced structural rigidity is attributed to strong hydrogen bonds between the phosphoryl groups and the ammonium cations of the piperazine-based linker.[30] While Al-CAU-67 exhibits pronounced structural changes at each transformation step, precluding single-crystal or topotactic transformations, the structural flexibility likely stems from the greater conformational freedom of the extended bipiperidine linker and weaker hydrogen bonding reflected in the longer hydrogen bonds compared to MIL-91. Exposure of the dehydrated phases of Al-MIL-91[30] as well as Al-CAU-67 (Figure 5) to humid air at room temperature results in complete and reversible rehydration and restoration of crystallinity.

SORPTION PROPERTIES

The high amount of removable water molecules up to 150 °C observed in the TG curve prompted us to study the adsorption of various probe molecules to gain information on the porosity, framework responsiveness, and guest-host interactions of Al-CAU-67 (Figure 4). Thermal activation (80 °C, $p < 10^{-2}$ kPa) of a water-loaded sample (Al-CAU-67-Reflux) resulted in a negligible N_2 uptake at 77 K, which was probably due to a framework collapse caused by capillary forces upon removal of the water molecules (SI section 4.7). To prevent the collapse, a stepwise activation protocol was developed

comprising sequential solvent exchange steps using MeOH, EtOH, and DCM, with the samples kept DCM-wet until final activation (80 °C, $p < 10^{-2}$ kPa). Microporosity was observed, but despite this careful protocol, structural changes during desolvation are still observed, consistent with the intrinsic flexibility of the framework.

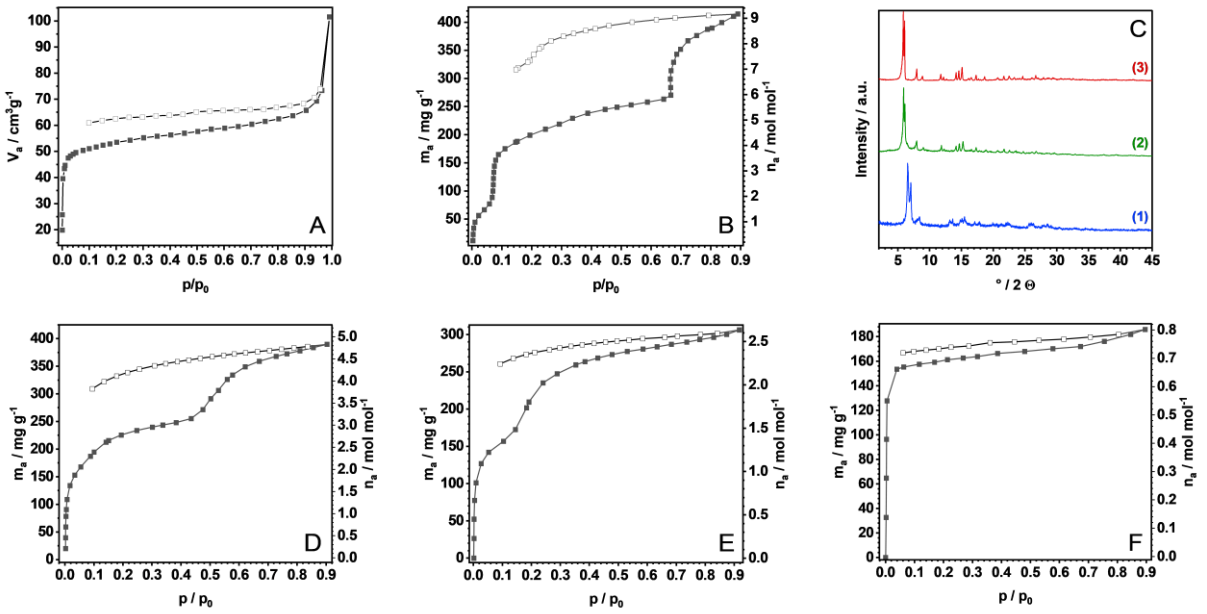

Figure 4: Sorption isotherms and PXRD patterns of Al-CAU-67. The adsorption (filled symbols) and desorption (open symbols) branches of the isotherms are shown. (A) Nitrogen gas and (B) water vapor sorption isotherms of Al-CAU-67-SE. (C) PXRD patterns of samples after N_2 sorption measurement (1, blue), stored for 48 h under ambient conditions (2, green) and after recycling, Al-CAU-67-Recycle (3, red) highlighting the structural changes upon activation and sorption measurement (1) as well as the possibility to regain long range order upon treatment with H_2O ((2) and (3)). (D) MeOH vapor sorption isotherm. (E) EtOH vapor sorption isotherm. (F) Toluene vapor sorption isotherm. SE = solvent exchanges, Recycle = reflux treatment in water.

Nitrogen sorption isotherms were recorded at 77 K to determine the specific surface area via the BET method, applying the Rouquerol criteria.[53] Water, MeOH, EtOH and toluene vapor sorption at 298 K were used to assess solvent uptake and to probe framework flexibility. Additional sorption measurements were performed using CO_2 at 298 K and Ar at 87 K. Al-CAU-67 exhibited porosity towards all tested adsorptives (Figure 4, Table 2, SI section 4.7).

The N_2 isotherm of Al-CAU-67-SE exhibits Type-I behavior with a BET surface area of 205 $m^2\ g^{-1}$, markedly lower than the theoretical value of 1084 $m^2\ g^{-1}$ calculated for the fully expanded structure (Poreblazer[54–56]). Similar results with Ar at 87 K (SI section 4) confirm that the reduced surface area originates from framework contraction during activation, in line with the VT-PXRD and solid-state NMR data. Water sorption data revealed a maximum uptake of 415 mg g^{-1} (≈ 9 H_2O per formula unit) in three distinct steps (2, 4, and 3 molecules), indicative of progressive pore filling and framework flexibility.

Kinetic limitations during rehydration are probably responsible for the smaller uptake compared to the results of the TG and elemental analysis; humidity-dependent PXRD data confirmed regeneration of the original framework upon equilibration (72 h, RH = 75 %, shown below). Vapor-sorption isotherms of MeOH, EtOH, and toluene demonstrate different sorption behaviors, reflecting the impact of the kinetic diameters (3.63, 4.53, 5.25 Å) and specific host-guest interactions. Maximum uptakes reach 389 mg g^{-1} (4.8 mol mol^{-1}) for MeOH, 306 mg g^{-1} (2.6 mol mol^{-1}) for EtOH, and 186 mg g^{-1} (0.8 mol mol^{-1}) for toluene. Alcohol sorption revealed sorbate-dependent transitions. H_2O, MeOH and EtOH vapor sorption experiments show multi-step isotherms, characteristic of adsorption-induced switching from narrow- to large-pore forms. The EtOH step occurs at lower p/p_0 values than the MeOH step, which can be rationalized either by the more hydrophobic nature of the pore or by the higher polarizability of EtOH, leading to stronger sorbate-sorbent and sorbate-sorbate interactions and thereby lowering the pressure required to trigger the transition. The smaller kinetic diameter of MeOH, however, enables slightly higher overall uptake. In contrast, toluene adsorption – with a much larger kinetic diameter and lacking hydrogen-bonding capability – results in a Type I isotherm, indicating strong interactions due to the more hydrophobic nature of the pore or high polarizability of the sorbate, adsorption into narrow pores of the activated framework and absence of an adsorption-triggered phase transition.

Table 2: Summary of physical parameters of selected gas and vapor adsorbates and the results of the sorption experiments of Al-CAU-67.

Probe	Kin. Diam[57]. / Å	Polarizability[57] X10^{25}/cm^{-1}	Dipole moment[57] x10^{18}/esu cm	Temp. / K	Isotherm	Specific surface area micropore volume uptake capacity
N_2	3.64-3.80	17.403	0	77	Type I	s_{BET} = 205 m^2/g V_{tot}=0.155 cm^3/g (p/p_0 = 0.99)
H_2O	2.641	14.5	1.855	298	Multistep	$m_{ads,\ max}$ = 415 mg/g $n_{ads,\ max}$ = 9 mol/mol
CO_2	3.3	29.11	0	298	Near linear	$n_{ads,\ max}$ = 404 mmol/mol (100 KPa)
Ar	3.542	16.411	0	87	Type I	s_{BET} = 202 m^2/g V_{tot}=0.089 cm^3/g (p/p_0 = 0.76)
MeOH	3.626	32.3 - 33.2	1.70	298	Multistep	$m_{ads,\ max}$ = 389 mg/g $n_{ads,\ max}$ = 4.8 mol/mol

EtOH	4.530	51.1 - 54.1	1.69	298	Multistep	$m_{ads,\ max}$ = 306 mg/g $n_{ads,\ max}$ = 2.6 mol/mol
Toluene	5.25	118 - 123	0.375	298	Type I	$m_{ads,\ max}$ = 185.85 mg/g $n_{ads,\ max}$ = 0.803 mol/mol

After the sorption experiments, PXRD patterns of the activated samples revealed structural changes upon activation, guest uptake, and release. Notably, long-range order can be fully recovered by storing the sample in humid air or by refluxing the material in water (Figure 4, SI), highlighting the reversible and flexible nature of the framework, in line with a displacive rather than reconstructive nature of the phase transition.

Details regarding the sorption behavior of Ga-CAU-67 are provided in the SI section 4.7.2.

SOLVENT-DRIVEN STRUCTURE CHANGES

To investigate the reversible structural breathing behavior[58–61] upon de- and rehydration, *in-situ* PXRD under controlled relative humidity (RH) was used to investigate framework changes upon water sorption (Figure 5). Prior to measurement, Al-CAU-67-SE was activated under dry N_2 at 80 °C for 3 h. Subsequently, the sample was exposed to incremental levels of relative humidity, selected to correspond to key features observed in the water-vapor adsorption isotherm.

Upon activation of Al-CAU-67, the most prominent reflections shift to higher 2θ values and markedly broaden, accompanied by the attenuation of weak reflections, consistent with the contraction of the unit cell and reduced long-range order in the dehydrated framework. At low RH (≤ 15 %), the diffractograms are dominated by reflections of this activated phase, in line with the modest uptake in the initial low p/p_0 regime of the isotherm (Figure 5). Between 15 - and 35 % RH, the reflections shift systematically toward lower 2θ values and additional reflections emerge, indicating lattice expansion and a hydration-induced change to accommodate the water molecules. Above 40 % RH, the patterns progressively revert toward those of the hydrated Al-CAU-67 phase, with a mixed-phase region across this RH window (RH = 40 – 70 %), where reflections of the dehydrated and hydrated structures as well as other phases coexist. The observation of phase mixtures could be due to the slow kinetics of the water uptake. After 30 h at 75 % RH, the PXRD pattern converges with that of the original hydrated material (Figure 5).

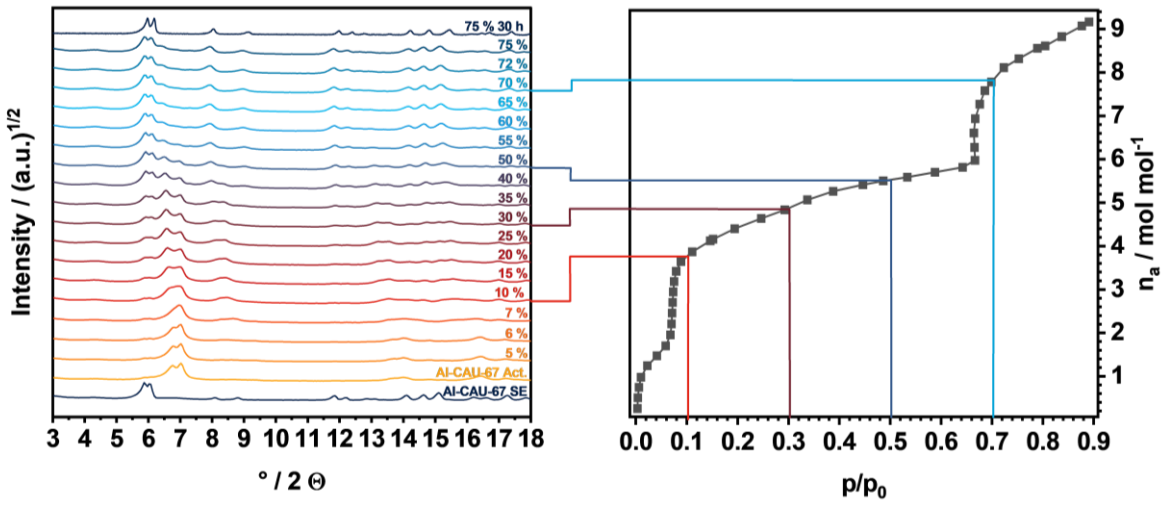

Figure 5: Humidity-dependent in situ PXRD (left) and water-vapor adsorption isotherm (right) of Al-CAU-67-SE. Before measurement, the sample was activated under dry N_2 (80 °C, 3 h). RH set points for PXRD were chosen to match characteristic regions of the isotherm (vertical guides). On activation, reflections shift to higher 2θ and broaden, consistent with unit-cell contraction and reduced long-range order. At low RH (≤ 15 %), the activated phase dominates. Between ~15-35 % RH, reflections move to lower 2θ and additional peaks appear, indicating lattice expansion and hydration-induced expansion. Above ~ 40 % RH, the patterns revert toward the hydrated phase with a mixed-phase region; after 30 h at 75 % RH, the pattern coincides with the hydrated material.

SOLID-STATE NMR INVESTIGATION

To gain further insight into the local coordination environments in Al-CAU-67, NMR crystallography was employed. The structure of Al-CAU-67 contains two distinct phosphonate groups (Figure 6 A), resulting in two sharp and well-resolved resonances in the **^{31}P MAS NMR** spectrum (Figure 6 B). The downfield resonance at 7.5 ppm corresponds to the P11-centered phosphonate group, while the upfield signal at -1 ppm arises from the P1-centered phosphonate. The chemical shift difference is attributed to a weaker hydrogen-bonding nature of the N11···H11···O2-P1 bond, driven by a longer bond distance, 2.8437(10) Å vs. 2.7881(14) Å for N1···H1···O12=P11, and the direct participation of a phosphoryl oxygen (P=O), which typically forms stronger hydrogen bonds than bridging oxygen atoms (P-O-M) (Figure 6 A). NMR simulations (SI section 4.8) of the O2-P1 (pink) and O12=P11 (blue) contributions closely match the experimental spectrum, confirming the assignment of these phosphorus environments (Figure 6 B). Following the post-synthetic reflux treatment, the resolution of the ^{31}P resonances increases, which can be attributed to reduced structural disorder resulting in more homogeneous phosphorus environments (SI section 4.8). Notably, such spectral sharpening is absent in the Al-MIL-91 framework (SI section 4.8.2). The **^{27}Al MAS NMR** spectrum of Al-CAU-67 (Al1 δ_{CS} = 8.2 ppm, CQ = 195.5 MHz and η_Q = 0.31; Al2: δ_{CS} = 4.9 ppm, CQ = 143.1 MHz and η_Q = 0.48) exhibits a characteristic second-order quadrupolar line shape, consistent with aluminum in sixfold-coordinated

(octahedra-like) environments (Figure 6 D, G).[48,62] To further resolve the individual Al sites, ^{27}Al triple-quantum magic angle spinning (**^{27}Al 3Q-MAS**) spectroscopy was employed (Figure 6 D). This technique effectively separates the isotropic chemical shift from quadrupolar broadening, enabling resolution of multiple sites within the material. The 3Q-MAS spectrum displays two prominent correlation regions, confirming the existence of two six-fold coordinated (AlO_6) sites, Al1 and Al2 (Figure 6 E, F). The isotropic signal at 8 ppm can be attributed to the Al1 site and correlates with the overall MAS spectrum, while the isotropic contribution around 5 ppm, assigned to Al2, specifically correlates with the MAS spectral region from 0 to -15 ppm. Fitted quadrupolar contour plots of each contribution (Figure 6 E, F) and the total spectrum (Figure 6 G, green) show good agreement with the experimental data, validating the structural model derived from SCXRD data and PXRD refinements.

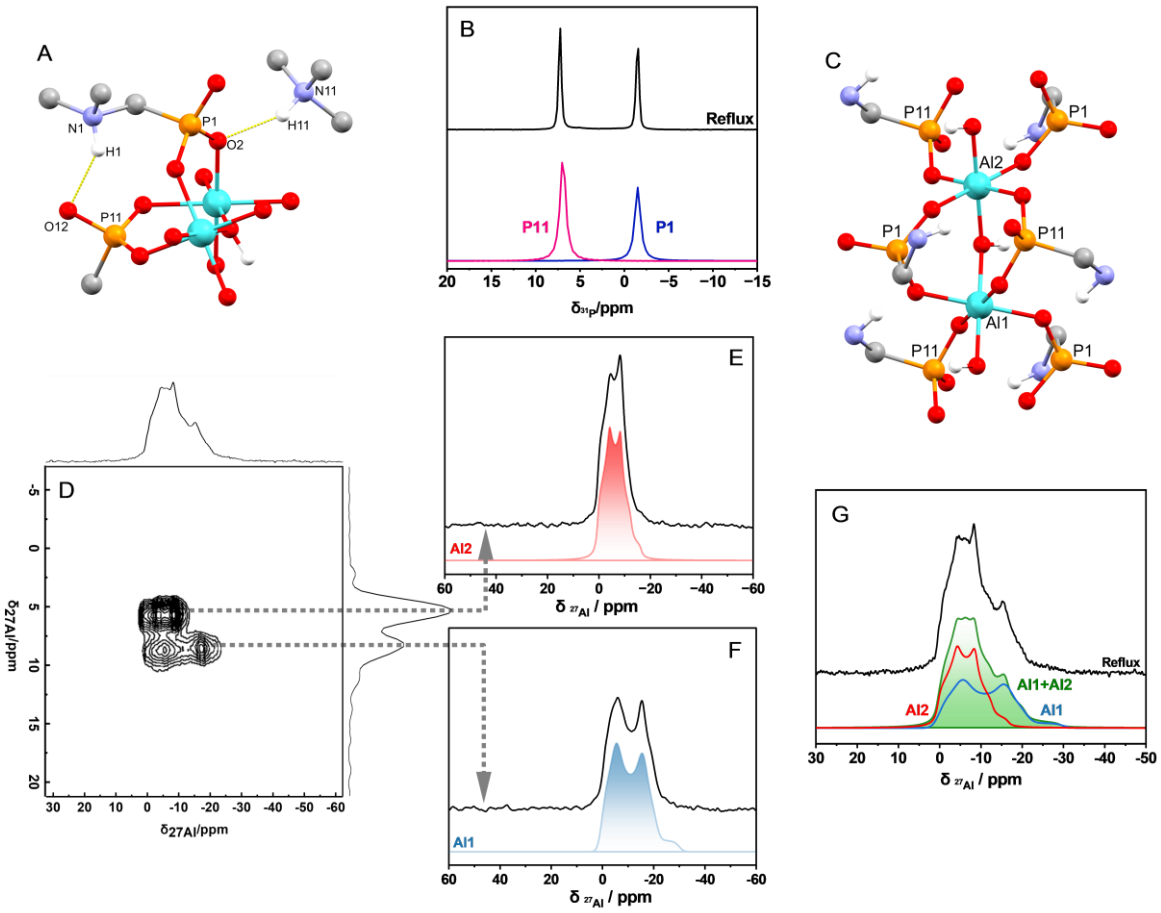

Figure 6: (A) Different bonding environments of P1 and P11. The single-bonded atom O2, which is connected to P1 and coordinating to Al2, forms a weaker H-bond compared to O12, which forms a double bond to P11. (B) ^{31}P MAS NMR spectrum of Al-CAU-67-Reflux (black) and simulation of the contributions of P1 (pink) and P11 (blue). (C) Different coordination environments of Al1 and Al2 resulting from the tilted polyhedra. (D) ^{27}Al 3Q-MAS NMR spectrum of Al-CAU-67. (E) Experimental slice of MQ-MAS correlation site at $\delta_{iso} \approx 5$ ppm (black) and contribution of Al2 (red). (F) Experimental slice of MQ-MAS correlation site at $\delta_{iso} \approx 8$ ppm (black) and contribution of Al1(blue). (G) 1D ^{27}Al MAS

spectrum (black) reproduced as the sum (green, Al1 + Al2) of the individually fitted contributions (Al2, red and Al1, blue).

The investigations in thermal and sorption properties revealed a highly flexible framework. In order to investigate the local structural changes accompanied by the changes of the magnetic environments, ssNMR experiments were carried out under *in-situ* activation conditions. Al-CAU-67-SE was dried at reduced pressure (< 10^{-2} kPa) for two hours and filled into the rotor under inert conditions, followed by *in-situ* activation at 80 °C using variable-temperature solid-state nuclear magnetic resonance (VT-ssNMR) spectroscopy. The ^{31}P and ^{27}Al ssNMR spectra acquired after activation at 80 °C (Figure 7: A, B, pink curves) revealed changes in the local atomic structure. These activation conditions also induce large structural changes, as evidenced by VT-PXRD measurements conducted under reduced pressure (Figure 7: C). The flexibility of Al-CAU-67 facilitates such structural changes, which influence the local environment of the phosphorus and aluminum atoms. At 80 °C, the ^{31}P NMR spectrum (Figure 7: A, pink curve) displays signals corresponding to a new local environment relative to the hydrated room-temperature data. This suggests a loss of symmetry in the framework as a result of structural changes upon guest removal. The altered chemical shifts of the P environments may correlate with a weakening of the hydrogen-bonding interactions within the framework and a higher flexibility of the linker. Similarly, the ^{27}Al NMR spectra at 80 °C (Figure 7: B, pink curve), exhibit changes, where these modifications predominately affect the Al1 site, indicating a decrease in quadrupolar coupling at this site.

To demonstrate the reversibility of these structural changes and the recovery of Al-CAU-67 to its initial state from a structural and crystallographic point of view, the activated material was subjected to a reflux treatment (Figure 7: A, B, C red curves). The resulting ^{27}Al and ^{31}P NMR spectra confirm the restoration of the original local environments.

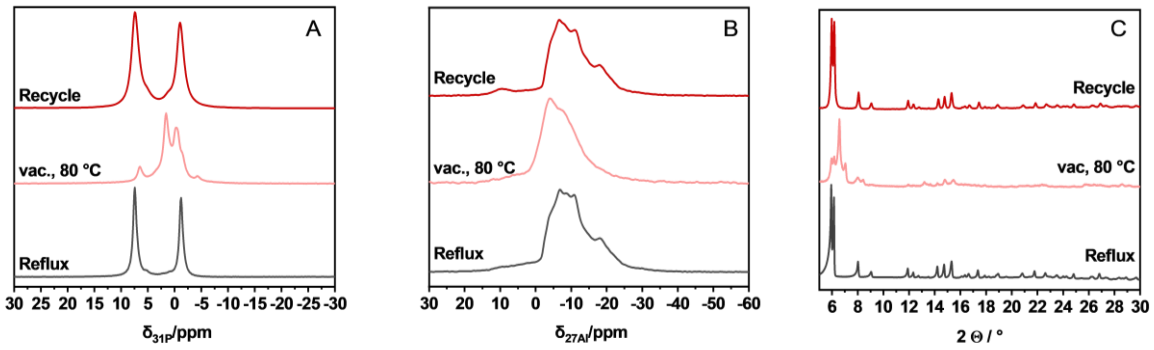

Figure 7: (A) ^{31}P MAS NMR spectrum of Al-CAU-67-Reflux (black), activated Al-CAU-67 at 80 °C under vacuum (pink) and recycled Al-CAU-67 after the reflux. (B) ^{27}Al MAS NMR spectrum of Al-CAU-67-Reflux (black), activated Al-CAU-67 at 80 °C under vacuum procedure (pink) and recycled Al-CAU-67 after the

reflux procedure. (C) PXRD data of Al-CAU-67-Reflux (black), activated Al-CAU-67 at 80 °C under vacuum (pink) and recycled Al-CAU-67 after the reflux procedure.

CONCLUSION

The synthesis and full characterization of CAU-67 [M(OH)(H_2BPD)] (M = Al^{3+}, Ga^{3+}) is presented. The compound forms an isoreticular structure previously reported for the metal phosphonate MIL-91 and thus presents a very rare example of an isoreticular expanded, porous metal phosphonate framework. As observed in Al-MIL-91, the framework is composed of chains of edge-sharing AlO_6 polyhedra linked in two dimensions by the bisphosphonate linker in a [2.110] fashion, resulting in a topology that is also commonly observed in metal carboxylate MOFs such as MIL-53. In analogy to MIL-91, the lattice is also stabilized by N H···O P hydrogen bonds between ammonium and phosphonate groups. Al-CAU-67 is microporous (s_{BET} ≈ 205 m^2 g^{-1}) and exhibits pronounced, reversible breathing (ΔV/V ≈ 32 %) between the hydrated and the activated state. Sorption experiments with vapors of water, MeOH, EtOH and toluene demonstrate size- and polarity-dependent guest uptake. $^{31}P/^{27}Al$ ssNMR data, including MQ-MAS measurements, validate two distinct P and Al sites, and can be used to clearly track the reversible breathing. Following temperature and pressure-induced changes through removal of guest molecules, the original phase is fully recovered by storage in air at 75% RH for a few days or by a 1h treatment in water under reflux conditions. Humidity- and VT-PXRD were used to map structural transformations, and in combination with DRIFTS and TGA data, the stability window of the dehydrated CAU-67 was established. The combination of high-throughput discovery, gram-scale synthesis, and comprehensive structure–property mapping establishes CAU-67 as a rare, well-characterized example of an expanded permanently porous phosphonate MOF.

SUPPORTING INFORMATION

The data that support the findings of this study are available in the supplementary material of this article. The authors have cited additional references within the Supporting Information.[30, 31]

AUTHOR CONTRIBUTIONS

J. Theissen and M. Radke designed the project, did formal analysis, conceptualization, data curation, methodology and investigation; M. Radke, J. Theissen, J. Lopau and J. Struve synthesized, analyzed, and characterized samples; J. Theissen and E. Derveaux carried out NMR measurements; J. Theissen performed VT- and humidity-dependent XRD; C. Näther performed SCXRD measurements and refinement; S. Mangelsen made the refinement of PXRD and PDF data; M. Radke and F. Steinke made refinement of PXRD data; R. M. N. Adams and F. Tielens performed simulations; N. Gys conducted XPS measurements; C. Nelle and S. Henke conducted DTA-TG and DSC investigations. M. Radke and

J. Theissen did the visualization. Funding acquisition by N. Stock, R. Ameloot and W. Marchal. Supervision by N. Stock, R. Ameloot and W. Marchal.

The manuscript was written with contributions from all authors.

CONFLICTS OF INTEREST

There are no conflicts to declare.

ACKNOWLEDGEMENTS

The authors acknowledge the Flemish Research Foundation (FWO Vlaanderen) for financial support in the frame of a travel grant for a long stay abroad at Kiel University (V429124N). This project received funding from the FWO and F.R.S.-FNRS (Belgium) under the Excellence of Science (EOS) program ("PHOSPORE" – EOS reference number: 40,007,504). This work was further supported by the state of Schleswig-Holstein (Germany), Hasselt University and FWO Vlaanderen via the Hercules projects AUHL/15/2 - GOH3816N and I001324N. The high-resolution scanning electron microscope with EDX detector is funded by the Deutsche Forschungsgemeinschaft (DFG, German Research Foundation) - 529613430 (DFGINST 257/717-1 FUGG).

We acknowledge the NMR core at Hasselt University and Sander Smeets, Elsy Thijssen for support with the ICP measurements, the European Synchrotron Radiation Facility (ESRF) for the provision of synchrotron radiation facilities under proposal number MA-6553 (DOI: 10.15151/ESRF-ES-2193756500), and we would like to thank Catherine Dejoie for assistance and support in using beamline ID22. We acknowledge Nattapol Ma and BL04B2 beamlines at SPring-8 for the synchrotron X-ray total scattering experiments with the approval of JASRI (Proposal No. 2024B1167).

The authors thank the spectroscopic division of the department of inorganic chemistry at Kiel University, namely Dr. Tobias Engesser, Stephanie Pehlke, Jacqueline Pick and Birgit Burghoff as well as the NMR division of the organic chemistry at Kiel University, namely Prof. Dr. Frank Sönnichsen, Ghaith Agha and Gitta Kohlmeyer-Yilmaz for their support with various measurements.

The authors thank Masaya Sugihara, Dr. Nicole Pienack and Dennis Egawa for support with the SEM pictures; Jesus Gandara Loe, Leen Boullart and Lorenzo Meneghin for the support during the beamtime at ESRF (ID22); Christoph Meier, Tobias Otto, Hauke Rohr and Bastian Achenbach for the sorption measurements.

DATA AVAILABILITY

The datasets used and/or analyzed during the current study are available from the corresponding author upon reasonable request. Supplementary information is available.

REFERENCES

(1) Furukawa, H.; Cordova, K. E.; O'Keeffe, M.; Yaghi, O. M. The chemistry and applications of metal-organic frameworks. *Science (New York, N.Y.)* **2013**, *341* (6149), 1230444. DOI: 10.1126/science.1230444.

(2) Maurin, G.; Serre, C.; Cooper, A.; Férey, G. The new age of MOFs and of their porous-related solids. *Chemical Society reviews* **2017**, *46* (11), 3104–3107. DOI: 10.1039/C7CS90049J.

(3) Bao, S.-S.; Shimizu, G. K.; Zheng, L.-M. Proton conductive metal phosphonate frameworks. *Coordination Chemistry Reviews* **2019**, *378*, 577–594. DOI: 10.1016/j.ccr.2017.11.029.

(4) Huang, Y.; Zhou, F.; Feng, J.; Zhao, H.; Qi, C.; Ji, J.; Bao, S.; Zheng, T. An ultra-stable hafnium phosphonate MOF platform for comparing the proton conductivity of various guest molecules/ions. *Chemical communications (Cambridge, England)* **2021**, *57* (10), 1238–1241. DOI: 10.1039/D0CC07375J.

(5) Zheng, T.; Yang, Z.; Gui, D.; Liu, Z.; Wang, X.; Dai, X.; Liu, S.; Zhang, L.; Gao, Y.; Chen, L.; Sheng, D.; Wang, Y.; Diwu, J.; Wang, J.; Zhou, R.; Chai, Z.; Albrecht-Schmitt, T. E.; Wang, S. Overcoming the crystallization and designability issues in the ultrastable zirconium phosphonate framework system. *Nature communications* **2017**, *8*, 15369. DOI: 10.1038/ncomms15369. Published Online: May. 30, 2017.

(6) Salcedo-Abraira, P.; Serrano-Nieto, R.; Biglione, C.; Cabrero-Antonino, M.; Vilela, S. M.; Babaryk, A. A.; Tilve-Martínez, D.; Rodriguez-Diéguez, A.; Navalón, S.; García, H.; Horcajada, P. Two Cu-Based Phosphonate Metal–Organic Frameworks as Efficient Water-Splitting Photocatalysts. *Chem. Mater.* **2023**, *35* (11), 4211–4219. DOI: 10.1021/acs.chemmater.3c00054.

(7) Gao, C.-Y.; Ai, J.; Tian, H.-R.; Wu, D.; Sun, Z.-M. An ultrastable zirconium-phosphonate framework as bifunctional catalyst for highly active CO2 chemical transformation. *Chemical communications (Cambridge, England)* **2017**, *53* (7), 1293–1296. DOI: 10.1039/C6CC08773F.

(8) Xie, H.; Atilgan, A.; Joodaki, F.; Cui, J.; Wang, X.; Chen, H.; Yang, L.; Zhang, X.; Son, F. A.; Idrees, K. B.; Wright, A. M.; Wells, J. L.; Morris, W.; Klein, J.; Franklin, L.; Harrington, F.; Herrington, S.; Han, S.; Kirlikovali, K. O.; Islamoglu, T.; Snurr, R. Q.; Farha, O. K. Hydrolytically Stable Phosphonate-Based Metal-Organic Frameworks for Harvesting Water from Low Humidity Air. *Small (Weinheim an der Bergstrasse, Germany)* **2025**, *21* (22), e2503178. DOI: 10.1002/smll.202503178. Published Online: Apr. 18, 2025.

(9) Mysore Ramesha, B.; Meynen, V. Advances and Challenges in the Creation of Porous Metal Phosphonates. *Materials (Basel, Switzerland)* **2020**, *13* (23). DOI: 10.3390/ma13235366. Published Online: Nov. 26, 2020.

(10) Groom, C. R.; Bruno, I. J.; Lightfoot, M. P.; Ward, S. C. The Cambridge Structural Database. *Acta crystallographica Section B, Structural science, crystal engineering and materials* **2016**, *72* (Pt 2), 171–179. DOI: 10.1107/S2052520616003954. Published Online: Apr. 1, 2016.

(11) Firmino, A. D. G.; Mendes, R. F.; Figueira, F.; Tomé, J. P. C.; Almeida Paz, F. A. Exceptional thermal stability of lanthanide-phosphonate frameworks. *J. Mater. Chem. C* **2024**, *12* (38), 15401–15407. DOI: 10.1039/D4TC02589J.

(12) Healy, C.; Patil, K. M.; Wilson, B. H.; Hermanspahn, L.; Harvey-Reid, N. C.; Howard, B. I.; Kleinjan, C.; Kolien, J.; Payet, F.; Telfer, S. G.; Kruger, P. E.; Bennett, T. D. The thermal stability of metal-organic frameworks. *Coordination Chemistry Reviews* **2020**, *419*, 213388. DOI: 10.1016/j.ccr.2020.213388.

(13) Gagnon, K. J.; Perry, H. P.; Clearfield, A. Conventional and unconventional metal-organic frameworks based on phosphonate ligands: MOFs and UMOFs. *Chemical reviews* **2012**, *112* (2), 1034–1054. DOI: 10.1021/cr2002257. Published Online: Nov. 29, 2011.

(14) Shearan, S. J.; Stock, N.; Emmerling, F.; Demel, J.; Wright, P. A.; Demadis, K. D.; Vassaki, M.; Costantino, F.; Vivani, R.; Sallard, S.; Ruiz Salcedo, I.; Cabeza, A.; Taddei, M. New Directions in Metal Phosphonate and Phosphinate Chemistry. *Crystals* **2019**, *9* (5), 270. DOI: 10.3390/cryst9050270.

(15) Patzschke, C.; Forsyth, C. M.; Batten, S. R.; Chaffee, A. L. Formation of a non-porous cobalt-phosphonate framework by small pH change in the preparation of the microporous STA-16(Co). *CrystEngComm* **2014**, *16* (28), 6296–6299. DOI: 10.1039/C4CE00509K.

(16) Zheng, T.; Tan, W.; Zheng, L.-M. Porous Metal Phosphonate Frameworks: Construction and Physical Properties. *Accounts of chemical research* **2024**, *57* (20), 2973–2984. DOI: 10.1021/acs.accounts.4c00337. Published Online: Oct. 7, 2024.

(17) Ondrušová, S.; Kloda, M.; Rohlíček, J.; Taddei, M.; Zaręba, J. K.; Demel, J. Exploring the Isoreticular Continuum between Phosphonate- and Phosphinate-Based Metal-Organic Frameworks. *Inorg. Chem.* **2022**, *61* (47), 18990–18997. DOI: 10.1021/acs.inorgchem.2c03271. Published Online: Nov. 11, 2022.

(18) Shannon, R. D. Revised effective ionic radii and systematic studies of interatomic distances in halides and chalcogenides. *Acta Cryst A* **1976**, *32* (5), 751–767. DOI: 10.1107/S0567739476001551.

(19) Lyubetskaya, T.; Korenaga, J. Chemical composition of Earth's primitive mantle and its variance: 1. Method and results. *J. Geophys. Res.* **2007**, *112* (B3). DOI: 10.1029/2005JB004223.

(20) McDonough, W. F.; Arevalo, R. Uncertainties in the composition of Earth, its core and silicate sphere. *J. Phys.: Conf. Ser.* **2008**, *136* (2), 22006. DOI: 10.1088/1742-6596/136/2/022006.

(21) Willhite, C. C.; Karyakina, N. A.; Yokel, R. A.; Yenugadhati, N.; Wisniewski, T. M.; Arnold, I. M. F.; Momoli, F.; Krewski, D. Systematic review of potential health risks posed by pharmaceutical, occupational and consumer exposures to metallic and nanoscale aluminum, aluminum oxides, aluminum hydroxide and its soluble salts. *Critical reviews in toxicology* **2014**, *44 Suppl 4* (Suppl 4), 1–80. DOI: 10.3109/10408444.2014.934439.

(22) Batra, I. P.; Kleinman, L. Chemisorption of oxygen on aluminum surfaces. *Journal of Electron Spectroscopy and Related Phenomena* **1984**, *33* (3), 175–241. DOI: 10.1016/0368-2048(84)80020-1.

(23) Poojary, M. D.; Hu, H.-L.; Campbell, F. L.; Clearfield, A. Determination of crystal structures from limited powder data sets: crystal structure of zirconium phenylphosphonate. *Acta Crystallogr B Struct Sci* **1993**, *49* (6), 996–1001. DOI: 10.1107/S0108768193006937.

(24) Alberti, G.; Costantino, U.; Allulli, S.; Tomassini, N. Crystalline Zr(R-PO3)2 and Zr(R-OPO3)2 compounds (R = organic radical). *Journal of Inorganic and Nuclear Chemistry* **1978**, *40* (6), 1113–1117. DOI: 10.1016/0022-1902(78)80520-X.

(25) Le Bideau, J.; Payen, C.; Palvadeau, P.; Bujoli, B. Preparation, Structure, and Magnetic Properties of Copper(II) Phosphonates. .beta.-CuII(CH3PO3), an Original Three-Dimensional Structure with a Channel-Type Arrangement. *Inorg. Chem.* **1994**, *33* (22), 4885–4890. DOI: 10.1021/ic00100a011.

(26) Maeda, K.; Akimoto, J.; Kiyozumi, Y.; Mizukami, F. Syntheses and crystal structures of two "organozeolites". In *Progress in Zeolite and Microporous Materials, Preceedings of the 11th International Zeolite Conference*; Studies in Surface Science and Catalysis; Elsevier, 1997; pp 197–204. DOI: 10.1016/S0167-2991(97)80556-3.

(27) Alberti, G.; Costantino, U.; Marmottini, F.; Vivani, R.; Zappelli, P. Zirconimphosphit-(3,3'5,5'-tetramethylbiphenyl)diphosphonat: ein mikroporöses anorganisch-organisches Polymer mit Sälen-Schichtstruktur. *Angewandte Chemie* **1993**, *105* (9), 1396–1398. DOI: 10.1002/ange.19931050928.

(28) Dines, M. B.; Cooksey, R. E.; Griffith, P. C.; Lane, R. H. Mixed-component layered tetravalent metal phosphonates/phosphates as precursors for microporous materials. *Inorg. Chem.* **1983**, *22* (6), 1003–1004. DOI: 10.1021/ic00148a036.

(29) Alberti, G.; Vivani, R.; Marmottini, F.; Zappelli, P. *Journal of Porous Materials* **1998**, *5* (3/4), 205–220. DOI: 10.1023/A:1009678120336.

(30) Serre, C.; Groves, J. A.; Lightfoot, P.; Slawin, A. M. Z.; Wright, P. A.; Stock, N.; Bein, T.; Haouas, M.; Taulelle, F.; Férey, G. Synthesis, Structure and Properties of Related Microporous N , N '-Piperazinebismethylenephosphonates of Aluminum and Titanium. *Chem. Mater.* **2006**, *18* (6), 1451–1457. DOI: 10.1021/cm052149l.

(31) Llewellyn, P. L.; Garcia-Rates, M.; Gaberová, L.; Miller, S. R.; Devic, T.; Lavalley, J.-C.; Bourrelly, S.; Bloch, E.; Filinchuk, Y.; Wright, P. A.; Serre, C.; Vimont, A.; Maurin, G. Structural Origin of Unusual

CO 2 Adsorption Behavior of a Small-Pore Aluminum Bisphosphonate MOF. *J. Phys. Chem. C* **2015**, *119* (8), 4208–4216. DOI: 10.1021/jp512596u.

(32) Wharmby, M. T.; Mowat, J. P. S.; Thompson, S. P.; Wright, P. A. Extending the pore size of crystalline metal phosphonates toward the mesoporous regime by isoreticular synthesis. *Journal of the American Chemical Society* **2011**, *133* (5), 1266–1269. DOI: 10.1021/ja1097995. Published Online: Jan. 7, 2011.

(33) Steinke, F.; Javed, A.; Wöhlbrandt, S.; Tiemann, M.; Stock, N. New isoreticular phosphonate MOFs based on a tetratopic linker. *Dalton transactions (Cambridge, England : 2003)* **2021**, *50* (38), 13572–13579. DOI: 10.1039/D1DT02610K. Published Online: Oct. 5, 2021.

(34) Reichenau, T. M.; Steinke, F.; Wharmby, M. T.; Näther, C.; Engesser, T. A.; Stock, N. Targeted Synthesis of a Highly Stable Aluminium Phosphonate Metal-Organic Framework Showing Reversible HCl Adsorption. *Angewandte Chemie (International ed. in English)* **2023**, *62* (26), e202303561. DOI: 10.1002/anie.202303561. Published Online: May. 17, 2023.

(35) Glavinović, M.; Perras, J. H.; Gelfand, B. S.; Lin, J.-B.; Spasyuk, D. M.; Zhou, W.; Shimizu, G. K. H. Microporous Metal-Phosphonates with a Novel Orthogonalized Linker and Complementary Guests: Insights for Trivalent Metal Complexes from Divalent Metal Complexes. *Chemistry (Weinheim an der Bergstrasse, Germany)* **2023**, *29* (17), e202203835. DOI: 10.1002/chem.202203835. Published Online: Feb. 15, 2023.

(36) Gelfand, B. S.; Huynh, R. P. S.; Mah, R. K.; Shimizu, G. K. H. Mediating Order and Modulating Porosity by Controlled Hydrolysis in a Phosphonate Monoester Metal-Organic Framework. *Angewandte Chemie (International ed. in English)* **2016**, *55* (47), 14614–14617. DOI: 10.1002/anie.201607745. Published Online: Oct. 21, 2016.

(37) Yaghi, O. M.; O'Keeffe, M.; Ockwig, N. W.; Chae, H. K.; Eddaoudi, M.; Kim, J. Reticular synthesis and the design of new materials. *Nature* **2003**, *423* (6941), 705–714. DOI: 10.1038/nature01650.

(38) Freund, R.; Canossa, S.; Cohen, S. M.; Yan, W.; Deng, H.; Guillerm, V.; Eddaoudi, M.; Madden, D. G.; Fairen-Jimenez, D.; Lyu, H.; Macreadie, L. K.; Ji, Z.; Zhang, Y.; Wang, B.; Haase, F.; Wöll, C.; Zaremba, O.; Andreo, J.; Wuttke, S.; Diercks, C. S. 25 Years of Reticular Chemistry. *Angewandte Chemie (International ed. in English)* **2021**, *60* (45), 23946–23974. DOI: 10.1002/anie.202101644. Published Online: Jul. 9, 2021.

(39) Shimizu, G. K. H.; Vaidhyanathan, R.; Taylor, J. M. Phosphonate and sulfonate metal organic frameworks. *Chemical Society reviews* **2009**, *38* (5), 1430–1449. DOI: 10.1039/B802423P. Published Online: Mar. 12, 2009.

(40) Gagnon, K. J.; Teat, S. J.; Beal, Z. J.; Embry, A. M.; Strayer, M. E.; Clearfield, A. Isoreticular Investigation into the Formation of Four New Zinc Alkylbisphosphonate Families. *Crystal Growth & Design* **2014**, *14* (7), 3612–3622. DOI: 10.1021/cg500568e.

(41) Harvey, H. G.; Herve, A. C.; Hailes, H. C.; Attfield, M. P. Synthesis, Crystal Structures, and Modifications of Novel Framework Gallium Diphosphonates. *Chem. Mater.* **2004**, *16* (19), 3756–3766. DOI: 10.1021/cm049607v.

(42) Del Gómez-Alcántara, M. M.; Cabeza, A.; Moreno-Real, L.; Aranda, M. A.; Clearfield, A. Microporous aluminum bisphosphonates. *Microporous and Mesoporous Materials* **2006**, *88* (1-3), 293–303. DOI: 10.1016/j.micromeso.2005.09.021.

(43) Tholen, P.; Zorlu, Y.; Beckmann, J.; Yücesan, G. Probing Isoreticular Expansions in Phosphonate MOFs and their Applications. *Eur J Inorg Chem* **2020**, *2020* (17), 1542–1554. DOI: 10.1002/ejic.201901291.

(44) Coelho, A. A. Whole-profile structure solution from powder diffraction data using simulated annealing. *J Appl Crystallogr* **2000**, *33* (3), 899–908. DOI: 10.1107/S002188980000248X.

(45) Coelho, A. A. TOPAS and TOPAS-Academic : an optimization program integrating computer algebra and crystallographic objects written in C++. *J Appl Crystallogr* **2018**, *51* (1), 210–218. DOI: 10.1107/S1600576718000183.

(46) Hermer, N.; Wharmby, M. T.; Stock, N. Re-Determination of the Crystal Structure of MIL-91(Al). *Zeitschrift fur anorganische und allgemeine Chemie* **2017**, *643* (2), 137–140. DOI: 10.1002/zaac.201600358. Published Online: Dec. 16, 2016.

(47) Coxall, R. A.; Harris, S. G.; Henderson, D. K.; Parsons, S.; Tasker, P. A.; Winpenny, R. E. P. Inter-ligand reactions: in situ formation of new polydentate ligands. *J. Chem. Soc., Dalton Trans.* **2000** (14), 2349–2356. DOI: 10.1039/B001404O.

(48) Loiseau, T.; Serre, C.; Huguenard, C.; Fink, G.; Taulelle, F.; Henry, M.; Bataille, T.; Férey, G. A rationale for the large breathing of the porous aluminum terephthalate (MIL-53) upon hydration. *Chemistry (Weinheim an der Bergstrasse, Germany)* **2004**, *10* (6), 1373–1382. DOI: 10.1002/chem.200305413.

(49) Millange, F.; Walton, R. I. MIL-53 and its Isoreticular Analogues: a Review of the Chemistry and Structure of a Prototypical Flexible Metal-Organic Framework. *Israel Journal of Chemistry* **2018**, *58* (9-10), 1019–1035. DOI: 10.1002/ijch.201800084.

(50) Cheetham, A. K.; Rao, C. N. R.; Feller, R. K. Structural diversity and chemical trends in hybrid inorganic-organic framework materials. *Chemical communications (Cambridge, England)* **2006** (46), 4780–4795. DOI: 10.1039/B610264F.

(51) Taddei, M.; Costantino, F.; Vivani, R. Synthesis and crystal structure from X-ray powder diffraction data of two zirconium diphosphonates containing piperazine groups. *Inorg. Chem.* **2010**, *49* (20), 9664–9670. DOI: 10.1021/ic1014048.

(52) Levenson, D. A.; Zhang, J.; Szell, P. M. J.; Bryce, D. L.; Gelfand, B. S.; Huynh, R. P. S.; Fylstra, N. D.; Shimizu, G. K. H. Effects of Secondary Anions on Proton Conduction in a Flexible Cationic

Phosphonate Metal–Organic Framework. *Chem. Mater.* **2020**, *32* (2), 679–687. DOI: 10.1021/acs.chemmater.9b03453.

(53) Rouquerol, F. *Adsorption by powders and porous solids*:*Principles, methodology and applications*, Second edition; Elsevier/Academic Press, 2014.

(54) Sarkisov, L.; Bueno-Perez, R.; Sutharson, M.; Fairen-Jimenez, D. Materials Informatics with PoreBlazer v4.0 and the CSD MOF Database. *Chem. Mater.* **2020**, *32* (23), 9849–9867. DOI: 10.1021/acs.chemmater.0c03575.

(55) Sarkisov, L.; Harrison, A. Computational structure characterisation tools in application to ordered and disordered porous materials. *Molecular Simulation* **2011**, *37* (15), 1248–1257. DOI: 10.1080/08927022.2011.592832.

(56) Sarkisov, L.; Kim, J. Computational structure characterization tools for the era of material informatics. *Chemical Engineering Science* **2015**, *121*, 322–330. DOI: 10.1016/j.ces.2014.07.022.

(57) Li, J.-R.; Kuppler, R. J.; Zhou, H.-C. Selective gas adsorption and separation in metal-organic frameworks. *Chemical Society reviews* **2009**, *38* (5), 1477–1504. DOI: 10.1039/b802426j. Published Online: Mar. 26, 2009.

(58) Alhamami, M.; Doan, H.; Cheng, C.-H. A Review on Breathing Behaviors of Metal-Organic-Frameworks (MOFs) for Gas Adsorption. *Materials (Basel, Switzerland)* **2014**, *7* (4), 3198–3250. DOI: 10.3390/ma7043198. Published Online: Apr. 21, 2014.

(59) Henke, S.; Schneemann, A.; Wütscher, A.; Fischer, R. A. Directing the breathing behavior of pillared-layered metal-organic frameworks via a systematic library of functionalized linkers bearing flexible substituents. *Journal of the American Chemical Society* **2012**, *134* (22), 9464–9474. DOI: 10.1021/ja302991b. Published Online: May. 23, 2012.

(60) Murdock, C. R.; Hughes, B. C.; Lu, Z.; Jenkins, D. M. Approaches for synthesizing breathing MOFs by exploiting dimensional rigidity. *Coordination Chemistry Reviews* **2014**, *258-259*, 119–136. DOI: 10.1016/j.ccr.2013.09.006.

(61) Rambabu, D.; Goossens, T.; Bakuru, V. R.; Apostol, P.; Mairesse, F.; Steenhaut, T.; Beaujean, P.; Mondal, S. K.; Guo, X.; Zhang, Y.; Pal, S.; Markowski, R.; Lin, X.; Xu, P.; Chanteux, G.; Kachmar, A.; Da Tie; Ramackers, A.; Frano, V.; Robeyns, K.; Kumar Maji, T.; Filinchuk, Y.; Champagne, B.; Vlad, A. Mixed proton-electron conductivity in a dynamic 3D metal-organic framework. *Chem* **2025**, 102590. DOI: 10.1016/j.chempr.2025.102590.

(62) Machac, P.; Alauzun, J. G.; Styskalik, A.; Debecker, D. P.; Mutin, P. H.; Pinkas, J. Synthesis of high surface area aluminophosphate and -phosphonate xerogels by non-hydrolytic sol-gel reactions. *Microporous and Mesoporous Materials* **2021**, *311*, 110682. DOI: 10.1016/j.micromeso.2020.110682.